Inorganic Chemistry
Article
pubs.acs.org/IC

Experimental and Theoretical Investigations on Structural and Vibrational Properties of Melilite-Type $Sr_2ZnGe_2O_7$ at High Pressure and Delineation of a High-Pressure Monoclinic Phase

S. Nagabhusan Achary,*[†] Daniel Errandonea,[‡] David Santamaria-Perez,[‡,§] Oscar Gomis,[∥]
Sadiqua J. Patwe,[†] Francisco Javier Manjón,[⊥] Placida Rodríguez Hernandez,[#] Alfonso Muñoz,[#]
and Avesh Kumar Tyagi[†]

[†]Chemistry Division, Bhabha Atomic Research Centre, Trombay, Mumbai 400085, India

[‡]Departamento de Física Aplicada-ICMUV, MALTA Consolider Team, Universidad de Valencia, Edificio de Investigación, C/Dr. Moliner 50, 46100 Burjassot, Valencia, Spain

[§]Earth, Planetary and Space Sciences Department, University of California Los Angeles, 595 Charles Young Drive East, 951567, Los Angeles, United States

[∥]Centro de Tecnologías Físicas: Acústica, Materiales y Astrofísica, MALTA Consolider Team and [⊥]Instituto de Diseño para la Fabricación y Producción Automatizada, MALTA Consolider Team, Universitat Politècnica de València, Camí de Vera s/n, 46022 València, Spain

[#]Departamento de Física, Instituto de Materiales y Nanotecnología, MALTA Consolider Team, Universidad de La Laguna, 38205 La Laguna, Tenerife, Spain

Supporting Information

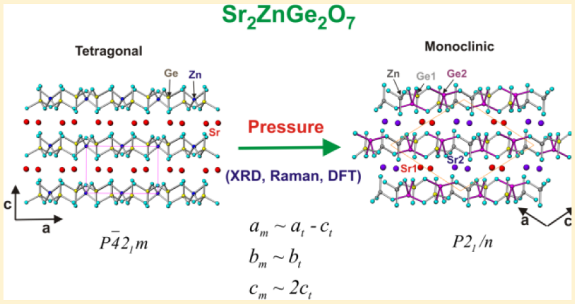

ABSTRACT: We report a combined experimental and theoretical study of melilite-type germanate, $Sr_2ZnGe_2O_7$, under compression. In situ high-pressure X-ray diffraction and Raman scattering measurements up to 22 GPa were complemented with first-principles theoretical calculations of structural and lattice dynamics properties. Our experiments show that the tetragonal structure of $Sr_2ZnGe_2O_7$ at ambient conditions transforms reversibly to a monoclinic phase above 12.2 GPa with ~1% volume drop at the phase transition pressure. Density functional calculations indicate the transition pressure at ~13 GPa, which agrees well with the experimental value. The structure of the high-pressure monoclinic phase is closely related to the ambient pressure phase and results from a displacive-type phase transition. Equations of state of both tetragonal and monoclinic phases are reported. Both of the phases show anisotropic compressibility with a larger compressibility in the direction perpendicular to the $[ZnGe_2O_7]^{2-}$ sheets than along the sheets. Raman-active phonons of both the tetragonal and monoclinic phases and their pressure dependences were also determined. Tentative assignments of the Raman modes of the tetragonal phase were discussed in the light of lattice dynamics calculations. A possible irreversible second phase transition to a highly disordered or amorphous state is detected in Raman scattering measurements above 21 GPa.

I. INTRODUCTION

Melilite and related materials have been of interest due to their exceptional optical properties, which make them suitable for important technological applications such as laser host and second harmonic generation,[1,2] as well as due to their ionic conduction[3] and magnetic properties.[4] They are also known for their mineralogical relevance[5−7] since natural melilite-type and melilite-related silicates are formed in igneous rock and have been known to form a wide variety of cation-substituted compositions while retaining their structure types.[6−8] In fact, a large number of compositions in nature crystallize within the parent tetragonal non-centrosymmetric (space group (SG) $P\bar{4}2_1m$) structure of melilite.[1] The general composition $A_2(T_1)_1(T_2)_2O_7$ with melilite-type structure has A cations with eightfold coordination and T_1 and T_2 cations with fourfold coordination.[1,2,9] The arrangements of tetrahedral units in melilite-type structures form nets of five-membered rings. The same coordination for T_1 and T_2 cations favors the intermixing of the cations of these two sites, and hence differences in local coordination around these sites have been observed in natural melilite-type and related structures.[7,10] The local distortion in the tetrahedral net and the A-site coordination play a crucial role in governing the topology of the tetrahedral units and final symmetry of the structure of such complex compounds.[5,9] Furthermore, local distortions in the cation polyhedra resulting

Received: April 28, 2015
Published: June 19, 2015

DOI: 10.1021/acs.inorgchem.5b00937
Inorg. Chem. 2015, 54, 6594−6605

from slightly different compositions are strongly reflected on materials properties, in particular, on the optical properties. Thus, the studies on melilite-type silicates and germanates with different compositions have also drawn a significant attention for stimulated emission as well as for second and third harmonic generation.[1,2,9]

Composition and temperature-induced commensurate to incommensurate structural transitions, arising from the modulation of tetrahedral units, lead to rich crystal chemistry in melilite-type materials.[11−14] Thus, structural studies on such materials under nonambient conditions, like temperature and pressure, have been performed in a number of related compounds.[11−23] Temperature-dependent structural studies have indicated an anisotropic thermal expansion behavior in melilite-type and related materials due to their layered structural arrangements, rigid nature of tetrahedral units, and flexible framework architect of rigid tetrahedra.[11,12,20,22,23] Moreover, temperature-dependent structural studies on a number of Ca^{2+}ion-bearing melilite-related compositions have revealed variable modulation parameters and temperatures for incommensurate to commensurate structural transition.[11,15] Interestingly, the non-centrosymmetric structure of the melilite structure is retained even at higher temperatures.

Compared to temperature-dependent studies, high-pressure (HP) studies on melilite-type materials are limited, and they are mainly focused on structural studies of silicates. The HP behavior of melilite-type silicate mineral, $Ca_2MgSi_2O_7$, has been reported, and a deviation in the unit cell volume at ∼1.33 GPa has been attributed to an incommensurate to commensurate phase transition.[21] No other structural transition up to 4 GPa, the maximum pressure of this study, has been observed.[21] Similar HP studies of melilite-related silicates, namely, $Sr_{2-x}Ba_xMgSi_2O_7$, indicate anisotropic compressibilities in them.[24,25] Furthermore, an inverse relationship between pressure and temperature has been explained from temperature- and pressure-dependent unit cell parameters.[24,25] Melilite-type $Ca_2MgSi_2O_7$ and $Ca_2Al_2SiO_7$ have been investigated up to 30 GPa, and a structural transition has been observed only in the former.[18] Besides, this study also confirmed the incommensurate to commensurate structural transition at ∼2 GPa in $Ca_2MgSi_2O_7$ and delineated a new phase transition from the melilite-type tetragonal phase (SG $P\bar{4}2_1m$) to the monoclinic phase (SG $P2_1/n$) above 20 GPa. However, Merilini et al. mentioned that the X-ray diffraction (XRD) patterns observed above 20 GPa still could be indexed on the parent tetragonal lattice.[18] The differences in the HP behavior of $Ca_2MgSi_2O_7$ and $Ca_2Al_2SiO_7$ have been assigned to the difference in the compressibility and distortion of the T_1 tetrahedral unit.[18]

Analogous to silicates, number of germanates of alkaline-earth metal ions also form melilite-type or related structure depending on the nature of other T_1 tetrahedral and/or A cations. In particular, Ca^{2+} and Sr^{2+} silicates and germanates crystallize in the tetragonal melilite-type (SG $P\bar{4}2_1m$) structure, while those of Ba^{2+} crystallize in the melilite-related monoclinic (SG $C2/c$) structure.[2] It can be mentioned here that both melilite-type and melilite-related $A_2(T_1)_1(T_2)_2O_7$ materials have different topologies in the planes formed by the $(T_2)_2O_7$ and $(T_1)O_4$ units. The differences in the orientations of the $(T_2)_2O_7$ units of the melilite-related materials make different types of rings, like four- and six-membered rings along with the five-memebered rings similar to the melilite-type compounds. The structural differences between these two classes of materials have been explained in literature.[5,24,25] The differences in the structures are reflected in the coordination polyhedra around the A^{2+} ions. It can be mentioned here that the structural studies on pyrosilicates and related materials have evidenced a number of symmetries: tetragonal, orthorhombic, triclinic, etc., depending on the nature and ionic radius of A-site cation.[24−26] Therefore, it is likely that tetragonal melilite-type materials could exhibit such structure-types at HP. However, such polymorphs have not been observed for melilite-type germanates either under pressure or temperature, perhaps due to the limited number of studies on germanates compared to analogous silicates. Furthermore, to the best of our knowledge, there has been no experimental Raman scattering (RS) study of melilites at HP, even in silicates.

To understand the behavior of melilite-type minerals at HP, in particular pyrogermanates, we performed in situ HP-XRD and HP-RS measurements on $Sr_2ZnGe_2O_7$ and compared them with our own theoretical calculations. HP-XRD and HP-RS results indicate a clear structural transition at ∼12 GPa, which according to HP-XRD could be a transition from a tetragonal to a monoclinic structure since the pattern of the HP phase is not indexable on the tetragonal lattice even though they appear closely similar. HP-RS measurements and lattice dynamics calculations allowed us to discuss the nature of the vibrational modes of the tetragonal melilite phase. Furthermore, HP-RS measurements support the HP transition to a phase with lower symmetry and have evidenced the coexistence of both low- and high-pressure phases. Finally, HP-RS measurements revealed a second structural transition likely to a disordered or amorphous phase above 21 GPa.

II. EXPERIMENTAL METHODS

Polycrystalline sample of $Sr_2ZnGe_2O_7$ was synthesized by solid-state reaction of appropriate amounts of $SrCO_3$ (99.9%, Aldrich), ZnO (99.5%, Aldrich), and GeO_2 (99.99%, Alfa-Aesar). A pellet of homogeneous mixture of the reactants was heated successively from 1073 to 1473 K with three intermittent grindings after each heating. After confirmation of the completion of the reaction, the product was rehomogenized and then pressed into pellets (∼1 cm diameter and 2 to 3 mm thickness). The pressed pellets were finally sintered at 1473 K for 24 h. The final sintered product was characterized by powder XRD study for phase purity and structure.

The powder XRD pattern at ambient pressure was recorded on a rotating anode-based X-ray diffractometer (Ragaku, Japan) using monochromatized Cu Kα radiation. The powder sample of $Sr_2ZnGe_2O_7$ was smeared on a glass sample holder using collodion as binder. The XRD data were collected from 10 to 100° with step width of 0.02° and using a time per step of 5 s. RS measurements at ambient pressure were performed in backscattering geometry with a Horiba JobinYvonLabRAMHRUV microspectrometer equipped with an edge filter and thermoelectric-cooled multichannel CCD detector. Measurements with a spectral resolution below 2 cm^{-1} were performed using the 632.8 nm line of the He−Ne laser for excitation with a laser power below 10 mW to avoid sample heating.

Angle-dispersive powder HP-XRD measurements on $Sr_2ZnGe_2O_7$ were performed with an Xcalibur diffractometer (Oxford Diffraction Limited) using Mo Kα X-ray. X-ray diffraction patterns were recorded on a 135 mm Atlas CCD detector placed at 110 mm from the sample. The X-ray beam was collimated to a diameter of 300 μm. HP measurements on $Sr_2ZnGe_2O_7$ powder were performed in a modified Merrill-Bassett diamond anvil cell (DAC) up to 19 GPa. The diamond anvils used for pressurization have 500 μm culets. The $Sr_2ZnGe_2O_7$ powder was placed in the 200 μm diameter holes of the stainless steel gasket pre-indented to a thickness of 50 μm. A mixture of methanol−ethanol−water with ratio of 16:3:1 was used as pressure-transmitting medium. Ruby chips evenly distributed in the pressure chamber were

DOI: 10.1021/acs.inorgchem.5b00937
Inorg. Chem. 2015, 54, 6594−6605

used to measure pressure by the ruby fluorescence method. Exposure time of each run was typically of 80 min. The DAC used for these experiments allows us to access an angular range of $4\theta = 50°$. The observed intensities were integrated as a function of 2θ to give conventional, one-dimensional diffraction profiles. The CrysAlis software, Version 171.34.49 (Oxford Diffraction Limited), was used for the data collections and the preliminary reduction of the data. The analyses of the powder XRD patterns were executed by using PowderCell[27] and Fullprof[28] software packages.

HP-RS measurements were performed on the previously described Raman micro-spectrometer by using small grains of a prepressed pellet inside the DAC with methanol−ethanol−water (16:3:1) as pressure-transmitting medium. Ruby fluorescence was used for the measurement of pressure. It was required to change the probing spot after two to three measurements due to diminishing of intensity because of degradation of sample by heat of the excitation laser with a power as low as 2 mW.

III. THEORETICAL CALCULATIONS

The first-principles total energy study of $Sr_2ZnGe_2O_7$ was performed within the density-functional theory (DFT) framework with the Vienna ab initio simulation package (VASP).[29] The generalized gradient approximation with PBEsol[30] prescription for the exchange-correlation energy, the projector-augmented wave pseudopotential,[31] and the plane-wave method were used. A kinetic energy cutoff of 520 eV and dense meshes of special k-points generated with the Monkhorst−Pack schemes[32] were employed to obtain highly accurate results. For the considered structures, a full optimization of all the structural parameters was performed at different selected volumes. In the optimized configurations the atomic forces on the atoms were lower than 0.005 eV/Å, and the differences between diagonal components of the stress tensor were less than 0.1 GPa (hydrostatic conditions). The equations of state for the studied structures were derived from the (E, V, P) theoretical data obtained for each of the selected volumes. The transition pressure and the relative phase stability of the considered structures were analyzed calculating the evolution of the enthalpy $H = E + PV$ with pressure.[33] The lattice-dynamic calculations of phonon modes were performed at the zone center (Γ point) of the BZ using the force-constant approach (or direct method).[33,34] The construction of the dynamical matrix at Γ point requires highly accurate calculations of the forces when fixed small displacements from equilibrium configuration of the atoms are considered. The number of independent displacements needed to obtain the dynamical matrix is reduced by using crystal symmetry. Diagonalization of this matrix provides the frequencies, symmetries, and polarization vectors as well as the irreducible representations and the character of the phonon modes at the Γ point.[33,34] The calculations do not include temperature effects and the zero point energy.

IV. RESULTS AND DISCUSSION

All reflections in the XRD pattern of $Sr_2ZnGe_2O_7$ recorded at the ambient pressure and temperature are attributable to the tetragonal melilite-type structure reported earlier [ICDD PDF 77−0433]. More detailed characterization of the sample was obtained by Rietveld refinement of the powder XRD data using the reported structural parameters of $Sr_2ZnGe_2O_7$.[35] The refined ambient powder XRD pattern of $Sr_2ZnGe_2O_7$ is shown in Figure 1. It can be mentioned here that no additional satellite reflections due to the incommensurate phase are observed in the present XRD pattern, and hence only the commensurate structure is concluded for $Sr_2ZnGe_2O_7$. It may be noted that among the melilite-type silicates and germanates, the incommensurate structure is more commonly observed in natural mineral samples, especially with Ca^{2+} ions compared to Sr^{2+} or Ba^{2+};[11,14,36,37] thus, smaller ionic radii of the Ca^{2+} ions might be a reason for the formation of the modulated structure. To observe any possible intermixing of tetrahedral cations, site occupations of the Zn^{2+} and Ge^{4+} were refined with a constraint of stoichiometry as $Sr_2ZnGe_2O_7$. No significant change in occupation of Zn^{2+} and Ge^{4+} sites are observed, and hence only the ordered melilite-type structure is considered in final refinements. The final refined structural parameters are summarized in Table 1, and they are in close agreement with the reported values.[35,36]

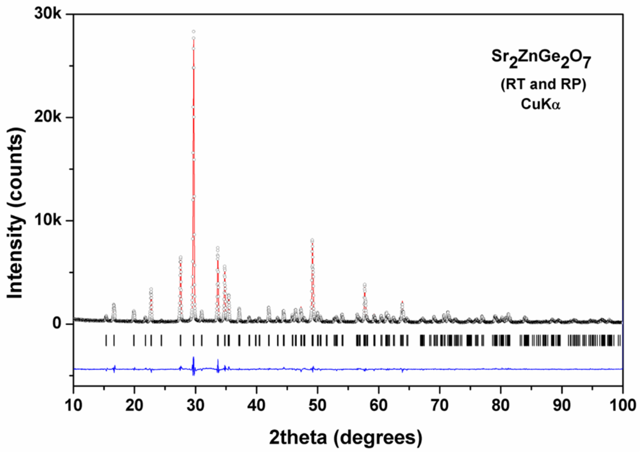

Figure 1. Powder XRD pattern of tetragonal $Sr_2ZnGe_2O_7$ at ambient pressure and temperature.

The analyses of the structural parameters at ambient conditions indicate that both Ge^{4+} and Zn^{2+} have tetrahedral coordination, and typical Ge−O distances are Ge−O1 = 1.754(4), Ge−O2 = 1.687(6), and Ge−O3 = 1.820(6) Å × 2, while the Zn−O distances are Zn−O3 = 1.881(6) Å × 4. From the bond length variations, it can be noticed that in $Sr_2ZnGe_2O_7$ the GeO_4 tetrahedra are distorted (distortion index $\Delta_d = 10.76 \times 10^{-4}$, defined as in ref 38), while the ZnO_4 tetrahedra are perfectly regular. The GeO_4 tetrahedral units are linked together by sharing one of the oxygen (O2) atoms forming the Ge_2O_7 unit, and they are linked by the ZnO_4 tetrahedral units. The corner-linked tetrahedra form a two-dimensional sheet with composition $[ZnGe_2O_7]^{2-}$, and they are held together by the Sr^{2+}ions. This arrangement leads to a flexible network of rigid polyhedra in the (001) plane, which are stacked along the [001] direction. Such arrangements are likely to give anisotropic elastic properties, and they are confirmed by the HP structural studies presented here.

Powder XRD patterns were recorded between ambient pressure and 19 GPa on increasing as well as on decreasing pressure. Typical powder XRD patterns recorded at some representative pressures are shown in Figure 2. Only data recorded below $2\theta = 18.3°$ are considered for further study because of the appearance of peaks due to the stainless steel gasket at higher angles. It can be noticed that all XRD patterns have almost similar features, but the peaks shift toward lower angle with increasing pressure due to the decrease in unit cell volume with pressure. Therefore, the melilite-type frame of the original sample seems to be retained up to the maximum pressure of this study. However, a close comparison of the XRD

Table 1. Structural Parameters of $Sr_2ZnGe_2O_7$ at Ambient Conditions

atoms		wyc	x^a	y^a	z^a	Biso (Å)^2	occ
Sr1	Sr^{2+}	4e	0.3337(1)	0.1663(1)	0.5066(3)	1.88(4)	1
			0.335 05	0.164 95	0.507 04		
Zn1	Zn^{2+}	2a	0.0000	0.000 00	0.000 00	2.06(8)	1
			0	0	0		
Ge1	Ge^{4+}	4e	0.1412(2)	0.3588(2)	0.9528(3)	1.81(5)	1
			0.143 37	0.356 63	0.953 38		
O1	O^{2-}	2c	0.500 00	0.000 00	0.169(2)	4.1(4)	1
			0.5	0	0.18302		
O2	O^{2-}	4e	0.1451(8)	0.3550(9)	0.2691(11)	3.3(2)	1
			0.138 15	0.361 85	0.277 86		
O3	O^{2-}	8f	0.0784(8)	0.1711(9)	0.7951(10)	2.7(2)	1
			0.082 39	0.178 08	0.790 71		

[a] The results calculated from DFT are shown in second row in each case. Tetragonal (SG $P\bar{4}2_1m$). $a = 8.1531(1)$, $c = 5.3256(1)$ Å, $V = 354.01(1)$ Å^3. ($R_p = 6.30\%$, $R_{wp} = 8.30\%$, $\chi^2 = 3.20$, $R_B = 4.91\%$). DFT-calculated values: $a = 8.1439$, $c = 5.3201$ Å, $V = 352.84$ Å^3.

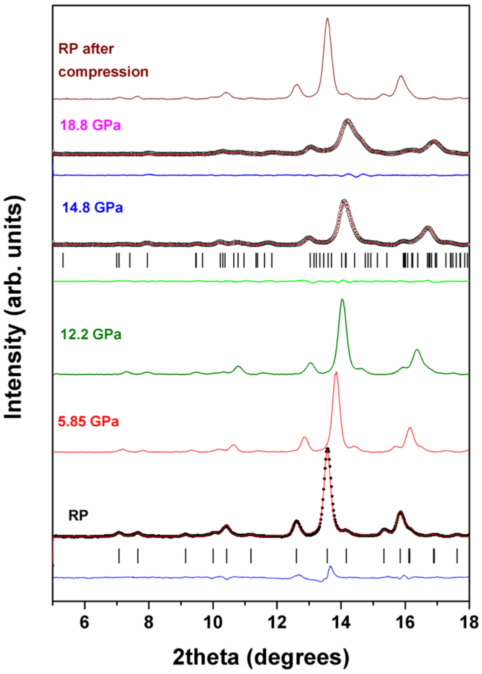

Figure 2. Powder XRD patterns of $Sr_2ZnGe_2O_7$ at some representative pressures. Fitted profiles for the XRD data at RP, 14.8, and 18.8 GPa are shown. The Bragg peak positions are shown as ticks, and difference plots are shown as continuous line below fitted profiles.

patterns shows that the XRD patterns recorded at and above 12.8 GPa show anomalous peak shifts compared to those observed below this pressure. Such anomalous peak shifts can be accounted for by a phase transition with feeble differences in structural arrangements between the original and the transformed phases and accompanied by a variation in lattice contraction. Similar features have been observed in pressure-induced scheelite to fergusonite and also in monazite to post monazite structural transitions due to the close similarity between the original and transformed structures.[39−41] Thus, the observed changes in the XRD patterns at ∼12.8 GPa can be attributed to a possible structural change, which will be commented later and confirmed by our HP-RS measurements.

It can be mentioned here that the pressure-transmitting medium methanol−ethanol−water (16:3:1) used in this study may behave non-hydrostatically above 10 GPa[42−44] and hence may influence the high-pressure behavior of the studied material. The non-hydrostaticity of pressure-transmitting medium can lead to a different structure than that observed under hydrostatic or quasi-hydrostatic conditions or conduct to different transition pressure. Such non-hydrostaticity-induced structural transitions have been reported for $HoVO_4$[45] and $CuWO_4$.[46] A large difference in the transition pressure due to non-hydrostaticity has been reported for Ti.[44] Non-hydrostatic effects can also influence the axial and bulk compressibility of the studied materials, in particular, when sample analyzed is intrinsically anisotropic as in the case of $Ca_2MgSi_2O_7$[18] and $Sr_2ZnGe_2O_7$ of the present study. To see the effect of non-hydrostaticity the pressure evolutions of experimental unit cell parameters of $Sr_2ZnGe_2O_7$, explained later in the manuscript, were compared with those calculated by DFT (which assumes total hydrostatic conditions). A good agreement between theoretical and experimental results suggests that the non-hydrostatic effects are not dominant in the HP behavior of $Sr_2ZnGe_2O_7$ within the pressure range covered by our experiments.

The analyses of the powder XRD data revealed that ambient-pressure tetragonal ($P\bar{4}2_1m$) structure is retained up to 12.2 GPa. The observed unit cell parameters of the low-pressure (LP) tetragonal phase of $Sr_2ZnGe_2O_7$ are $a = 8.1458(2)$ and $c = 5.3126(2)$ Å (at 0.21 GPa; the residuals of refinements $R_p = 1.81\%$, $R_{wp} = 2.89\%$); $a = 7.8915(4)$ and $c = 5.1315(4)$ Å (at 12.2 GPa; $R_p = 9.84\%$, $R_{wp} = 10.32\%$). As expected, the tetragonal structure has larger compression along the *c*-axis than along the *a*- and *b*-axes. Also, it is seen that the unit cell parameters observed in upstroke as well as downstroke are consistent. The pressure evolution of *a*- and *c*-parameters of the tetragonal phase shows nonlinear compressibility, and they are shown in Figure 3. The axial compressibilities (defined for a given dimension x as $\kappa_x = -(\partial \ln x/\partial P)$) are $\kappa_a = \kappa_b = 2.62(9) \times 10^{-3}$ GPa^{-1} and $\kappa_c = 2.98(9) \times 10^{-3}$ GPa^{-1} (Table 2). It can be mentioned here that the axial compressibilities calculated from the experimental unit cell parameters obtained in the quasi-hydrostatic range, that is, at $P < 10$ GPa, are within the error bars of these values. This confirms no significant effect of non-hydrostatic pressure-transmitting medium on the HP behavior of $Sr_2ZnGe_2O_7$.The compressibility ratio κ_c/κ_a for tetragonal $Sr_2ZnGe_2O_7$ as observed from the experimental study is 1.11, which is close to that (1.18) observed by Merlini et al.[18] for tetragonal $Ca_2MgSi_2O_7$. The compressibility ratio as calculated by ab initio calculations for tetragonal $Sr_2ZnGe_2O_7$ of the present study is 1.09. The close agreement of theory and

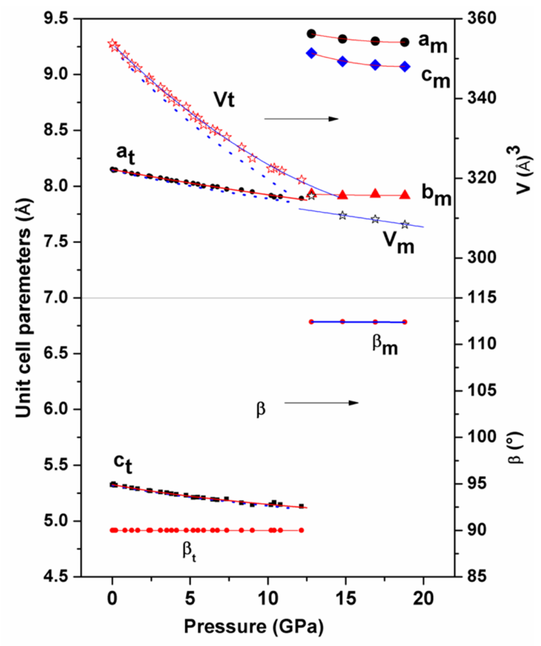

Figure 3. Pressure evolutions of unit cell parameters of LP and HP phases of $Sr_2ZnGe_2O_7$. Solid lines indicate third-order BM fit for LP phase. For monoclinic phase half of the unit cell volume is shown for comparison. The DFT-calculated parameters for LP phase are shown as dotted line. Polynomial fits of the pressure evolutions of unit cell parameters of HP phase are shown as solid line.

Table 2. Axial and Volume Compressibilities of LP and HP Phases of $Sr_2ZnGe_2O_7$

	LP-$Sr_2ZnGe_2O_7$ ($P\bar{4}2_1m$)	HP-$Sr_2ZnGe_2O_7$ ($P2_1/n$)
k_a (GPa^{-1})	$2.62(9) \times 10^{-3}$	$1.4(1.2) \times 10^{-3}$
k_b (GPa^{-1})		$0.4(0.8) \times 10^{-3}$
k_c (GPa^{-1})	$2.98(9) \times 10^{-3}$	$2.2(1.0) \times 10^{-3}$
k_β (GPa^{-1})		0.0(8)
K_V (GPa^{-1})	$7.9(7) \times 10^{-3}$	$3.8(2.0) \times 10^{-3}$

experiment suggests that the non-hydrostatic effects are not dominant in the HP behavior of $Sr_2ZnGe_2O_7$ within the pressure range covered in the experiments. The variations of *a*- and *c*-parameters with pressure are represented as the following nonlinear equations:

$$a(\text{Å}) = 8.149(2) - 0.026(1) \times P + 0.00034(7) \times P^2$$

$$c(\text{Å}) = 5.327(2) - 0.025(1) \times P + 0.00073(10) \times P^2$$

where *P* is the pressure in GPa.

As it was already commented, the analyses of the XRD pattern of $Sr_2ZnGe_2O_7$ recorded above 12.8 GPa revealed the presence of a transformed phase, from here onward named as HP phase. The observed reflections could be indexed in a monoclinic unit cell. Considering the different possible SGs of melilite-type minerals and analogous materials, like $K_2SrP_2O_7$ (SG $P2_1/c$),[47] $Ba_2ZnSi_2O_7$ (SG $C2/c$),[35] $Ca_2MgSi_2O_7$ (SG $P2_1/n$),[18] etc., the full XRD pattern at 12.8 GPa could be successfully refined and fitted with a monoclinic ($P2_1/n$) structure as the HP phase (residuals of refinements are R_p = 7.24%, R_{wp} = 10.20%). The refined unit cell parameters of HP phase at 12.8 GPa are *a* = 9.36(1), *b* = 7.93(1), *c* = 9.19(1) Å, and β = 112.4(1)°. To understand the structure of the HP phase the observed unit cell parameters were compared with reported unit cell parameters of various melilite-related materials and found to be close to those reported for cobalt (Co^{2+})-substituted $Ca_2ZnGe_2O_7$.[48] They are also closely similar to the monoclinic $P2_1/n$ phase of $Ca_2MgSi_2O_7$ reported by Merlini et al.[18] Thus, it is concluded that the tetragonal low-pressure (LP) phase of $Sr_2ZnGe_2O_7$ transforms to a monoclinic HP phase similar to that reported by Merlini et al.[18] for $Ca_2MgSi_2O_7$. Because of limited range and low resolution of experimental data in addition to the possible non-hydrostaticity of pressure transmission medium at $P > 12$ GPa, no precise structural parameters could be obtained for the HP phase.

Thus, to further understand the HP structural behavior and structure of HP phase, ab initio calculations within the density functional theory formalism were performed. At normal pressure, the calculated unit cell parameters of LP phase of $Sr_2ZnGe_2O_7$ are *a* = 8.1439, *c* = 5.3201 Å, and *V* = 352.84 Å^3, which are in close agreement with experimental values. The calculated position coordinates for the LP phase are included in Table 1 for comparison, which also show a close agreement. The pressure-dependent unit cell parameters of LP phase are shown as continuous dotted lines in Figure 3. The calculated unit cell parameters at higher pressure show a smooth decrease along both *a*- and *c*-axes, and they are comparable to the experimental values. Density functional theory calculation on the HP phase suggests two possible monoclinic structures, namely, $P2_1/n$ (*a* = 9.4507, *b* = 7.6914, *c* = 8.9859 Å, β = 113.28°; *Z* = 8) and $C2/c$ (*a* = 8.0759, *b* = 10.1981, *c* = 8.2254 Å, β = 116.17°, *Z* = 4). In both the monoclinic structures, the Sr atoms are eight-coordinated with oxygen atoms, while Ge and Zn are tetrahedrally coordinated with oxygen atoms. The polyhedra around the metal ions in the $P2_1/n$ structure are strongly distorted compared to that in the $C2/c$. However, the experimentally observed unit cell parameters are close to the structural parameters calculated for monoclinic $P2_1/n$ structure. The calculated position coordinates for the HP phase are given in Table 3, which shows a reasonably good agreement with the experimental values.[18] Further to observe the pressure-induced structural transition, the free energy difference between the tetragonal (LP) and monoclinic (HP) structures was calculated for $Sr_2ZnGe_2O_7$. The variation of free energy difference with pressure (Figure 4) indicates that the monoclinic ($P2_1/n$) structure of $Sr_2ZnGe_2O_7$ becomes stable above 13 GPa, which

Table 3. Structural Parameters of High-Pressure Phase of $Sr_2ZnGe_2O_7$[a] as Calculated by Density Functional Theory

atom	Wyc	*x*	*y*	*z*
Sr1	4*e*	0.2920	0.9470	0.1970
Sr2	4*e*	0.0196	0.7358	0.4479
Zn	4*e*	0.1050	0.9227	0.8211
Ge1	4*e*	0.2017	0.5641	0.8666
Ge2	4*e*	0.0655	0.2484	0.9638
O1	4*e*	0.1485	0.4597	0.9861
O2	4*e*	0.3713	0.4702	0.8726
O3	4*e*	0.0473	0.5547	0.6833
O4	4*e*	0.2882	0.1298	0.0622
O5	4*e*	0.0684	0.1678	0.1477
O6	4*e*	0.2648	0.7649	0.9569
O7	4*e*	0.9040	0.2465	0.7865

[a] SG $P2_1/n$. Unit cell parameters: *a* = 9.4508, *b* = 7.6914, *c* = 8.9859 Å, β = 113.28°, *V* = 600.01 Å^3. Experimental values at 18.8 GPa, *a* = 9.288, *b* = 7.915, *c* = 9.072 Å, β = 112.38°, *V* = 616.75 Å^3.

further supports the transition pressure found by diffraction and Raman studies.

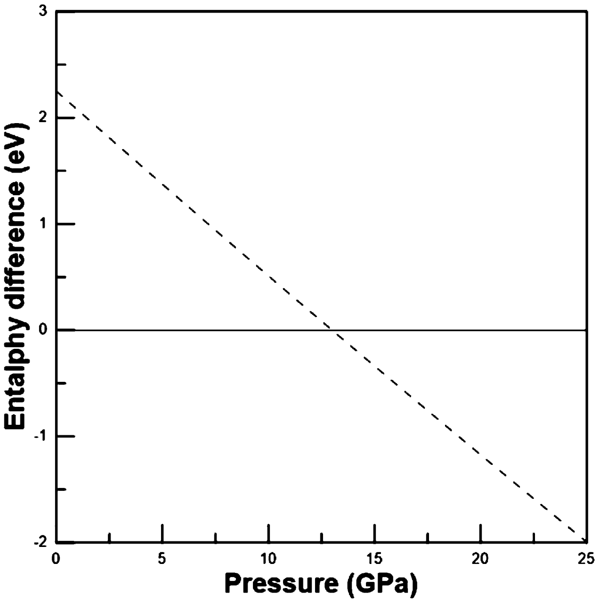

Figure 4. Variation of the difference in enthalpy of monoclinic HP and tetragonal LP phase with pressure. The enthalpy of tetragonal phase is shown as horizontal reference line.

The refined unit cell parameters of HP phase observed at 18.8 GPa are $a = 9.29(1)$, $b = 7.92(1)$, $c = 9.07(1)$ Å, and $\beta = 112.4(1)°$. The residuals of refinements of the XRD data recorded at 18.8 GPa are $R_p = 7.29\%$, $R_{wp} = 11.24\%$. The variations of unit cell parameters of the HP phase are included in Figure 3. The axial compressibilities of both HP phases of $Sr_2ZnGe_2O_7$ are determined from the experimental unit cell parameters, and they are summarized in Table 2. A comparison indicates that the HP phase is much less compressible than the LP phase. In addition, in the LP phase the behavior is nearly isotropic as observed from both theoretical and experimental data, while in the HP phase, the axial compressibilities differ very much one from the other. In particular, the lowest compressibility of the crystal structure is along the *b*-direction. Indeed, the value of κ_b in the HP phase (see Table 2) is as small as the linear incompressibility of diamond and other ultra-incompressible materials.[49,50] On the other hand the most compressible axis of the HP phase is the *c*-axis, which has a linear compressibility 1 order of magnitude larger than the *b*-axis (see Table 2). Additionally, we found that the monoclinic β angle of the HP phase is apparently not affected by compression. Finally, the volume drop at the structural transition is ~1%; that is, it is within the error margin of our data. This small value supports for the displacive nature of the phase transition due to the structural closeness of both LP and HP phases. The pressure-induced unit cell transformation from tetragonal to monoclinic phase can be related by unit cell relations as

$$\begin{pmatrix} a_m \\ b_m \\ c_m \end{pmatrix} = \begin{pmatrix} 1 & 0 & -1 \\ 0 & 1 & 0 \\ 0 & 0 & 2 \end{pmatrix} \begin{pmatrix} a_t \\ b_t \\ c_t \end{pmatrix}$$

where the subscripts *m* and *t* indicate monoclinic and tetragonal unit cells.

Typical comparison of the LP and HP structures is shown in Figure 5. A comparison of the LP and HP structures suggests closely similar structural arrangements of atoms in both, except the Sr and Ge as well as oxygen atoms split in the latter. The LP and HP structures can be directly compared by viewing them along the direction perpendicular to the stacking direction, that is, along [001] direction of tetragonal structure and [101] direction of the monoclinic structure. The analyses of the calculated structural parameters of monoclinic $Sr_2ZnGe_2O_7$

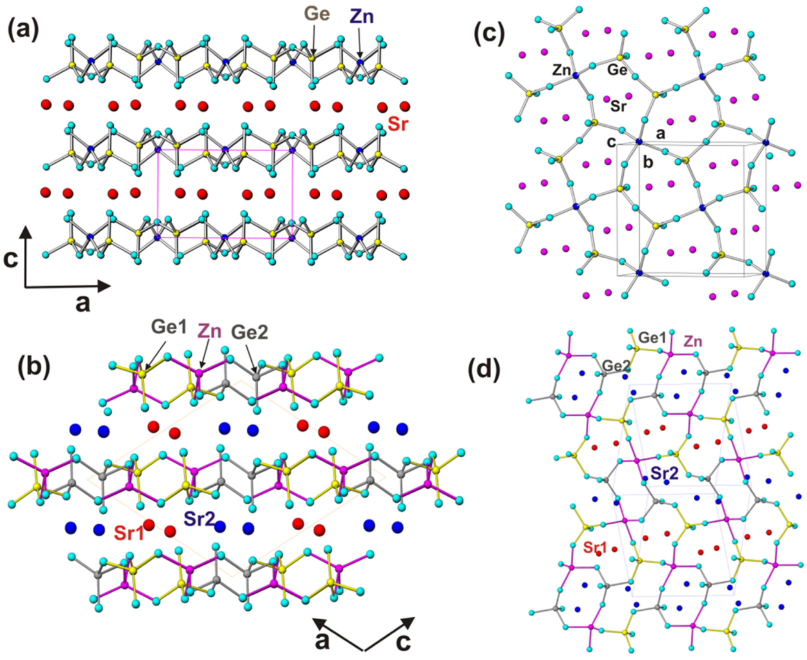

Figure 5. Crystal structures of $Sr_2ZnGe_2O_7$. (a) LP tetragonal ($P\bar{4}2_1m$, 010 projection) and (b) HP monoclinic ($P2_1/n$; 010 projection). Typical views of the $ZnGe_2O_7$ sheets in the LP and HP phases are shown in (c) 001 projection and (d) 101 projection, respectively.

revealed two types of Sr (Sr1 and Sr2), one Zn (Zn1), and two types of Ge (Ge1 and Ge2) in the structure. Both the Ge1 and Ge2 are tetrahedrally coordinated with typical bond lengths in the range from 1.739 to 1.783 Å, while the tetrahedral Zn1 has bond lengths in the 1.877 to 1.953 Å range. The structural parameters of monoclinic $Ca_2MgSi_2O_7$ reported by Merlini et al.[18] indicated similar coordination polyhedra around the Si and Mg atoms. However, in the monoclinic $Sr_2MgSi_2O_7$, the MgO_4 tetrahedron has larger distortion; specifically, the typical Mg−O bonds lengths are in between 1.85 and 2.29 Å. The refinement of position coordinates of the present observed XRD data of HP-phase revealed a similarly larger dispersion of bond lengths around the ZnO_4 tetrahedra (1.90 to 2.32 Å) and also an additional long bond (Zn−O7) at ~2.61 Å. This contradicts the observed more regular bond around all the atoms in theoretically calculated structure of monoclinic $Sr_2ZnGe_2O_7$. This deviation of theory and experiment can be attributed to the non-hydrostatic conditions of pressure-transmitting medium above 12 GPa and/or low resolution of the experimental data. Thus, only the profiles of XRD patterns of the HP phases were refined with theoretically calculated position coordinates to obtain unit cell parameters of HP-phase. The model biased fitted profiles for HP XRD patterns are given in Figure 2.

It can be observed that a pressure-induced structural distortion occurs at the phase transformation pressure where ZnO_4 and GeO_4 units basically retain their coordination but are distorted. Further it can be noticed the structural transformation also affects the network topology of the tetrahedral units. The analyses of structural parameters obtained from theory (in hydrostatic condition) indicated the topology of $[ZnGe_2O_7]$ layer ((001) plane of LP and (101) plane of HP $Sr_2ZnGe_2O_7$ phase) show clear differences. The orientations of the tetrahedral ZnO_4 and pyrogermanate (Ge_2O_7) units transformed from identical five-membered ring-type arrangements of LP-phase to different types of rings, like four- and six-membered rings along with the five-memebered rings in HP-phase. The transformed topology is similar to various melilite-related compounds reported in literature.[5,24,25]

The variations of unit cell volume with pressure for the LP and HP phases of $Sr_2ZnGe_2O_7$ are shown in Figure 3. For comparison half of the unit cell volume for the HP phase is shown in Figure 3. The volume drop at the structural transition is ~1%, that is, within the error margin of our data, and it is in agreement for the displacive nature of the phase transition. The pressure−volume data of LP phase was fitted with the third-order Birch−Murnaghan (BM) equation of state (EOS), and the obtained EOS parameters are V_0 = 353.9(2) Å^3, B_0 = 85(4) GPa, and B'_0 = 6.1(8). The implied value for B''_0 is −0.1223 GPa^{-1}. The DFT-calculated pressure-dependent unit cell volume (included in Figure 3) for LP phase was fitted to fourth-order BM, and the obtained EOS parameters are V_0 = 353.27 Å^3, B_0 = 83.08 GPa, B_0' = 3.997, and B_0'' = −0.171. These values are in good agreement with the experimental values. Because of the limited experimental data points for the HP phase, the EOS parameters could not be determined accurately. The calculated EOS parameters of the HP phase are V_0 = 643.98 Å^3, B_0 = 88.6 GPa, B_0' = 4.29, and B_0'' = −0.0482. A small increase in bulk modulus in the tetragonal to monoclinic phase is observed.

A comparison of the variation of unit cell volumes of the tetragonal and monoclinic phases indicates that the tetragonal phase has larger compressibility than the monoclinic phase (Figure 3). The volume compressibilities of these two phases are 7.98×10^{-3} GPa^{-1} (tetragonal; room pressure (RP) to 12.2 GPa) and 3.78×10^{-3} GPa^{-1} (monoclinic; 12.8 to 18.8 GPa). The larger difference can be accounted for by the relatively closely packed structural arrangement in the HP phase. The observed bulk modulus (85(4) GPa) of tetragonal phase of $Sr_2ZnGe_2O_7$ is comparable with those reported for analogous tetragonal melilites-type materials, like $Ca_2MgSi_2O_7$ (90(2) GPa,[21] 94(1) GPa[22]), $Sr_2MgSi_2O_7$ (107(3) GPa[25]), and $Ba_2MgSi_2O_7$ (122 GPa[25]). The comparable compressibility of melilite-type materials are thus related to their similar structural arrangements. More detailed analyses of structural parameters of tetragonal phase suggest that the compressibility mainly arises from the compression of the AO_8 polyhedra compared ZnO_4 or GeO_4 tetrahedra, which is as expected for the rigid nature of the latter. High-pressure studies of number of germanates and silicates as well as tungstates and molybdates indicate rigid nature of the tetrahedral units, while the compressibilities are mainly governed by larger polyhedra with higher coordination numbers.[40,41,51,52] A case study, like $ThGeO_4$ polymorphs shows rigid nature of GeO_4tetrahedra, and only the distortion and volume of ThO_8 units varies with pressure.[40] Similar studies on scheelite-type $SrWO_4$ or $SrMoO_4$ indicates the SrO_8 polyhedra are more compressible compared to the WO_4 or MoO_4 tetrahedral units.[51,52] Thus, it can be concluded that compressibility of $Sr_2ZnGe_2O_7$ is controlled by SrO_8 units.

To further understand the pressure evolution of structure and phase transition in melilite-type $Sr_2ZnGe_2O_7$, we performed in situ HP-RS studies up to 24 GPa. The structure of $Sr_2ZnGe_2O_7$ ($P\overline{4}2_1m$; point group D_{2d}^3) has two formula units per unit cell. Zn atoms are at 2*a* Wyckoff sites, O1 atoms are at 2*c* sites, Sr, Ge, and O2 atoms are located at 4*e* sites, and O3 atoms are at 8*f* sites. Therefore, group theoretical analyses predict 72 zone-center vibrational modes with mechanical representation: $\Gamma = 10A_1 + 6A_2 + 7B_1 + 11B_2 + 19E$, being E modes doubly degenerated. Of these vibrations, three are three acoustic modes (B_2 + E) and 69 optical modes ($\Gamma_{op} = 10A_1 + 6A_2 + 7B_1 + 10B_2 + 18E$). Since A_2 modes are silent, there are a total of 63 optical modes distributed into 63 Raman-active (R) modes ($\Gamma_R = 10A_1 + 7B_1 + 10B_2 + 18E$) and 46 infrared-active (IR) modes ($\Gamma_{IR} = 10B_2 + 18E$), leading to 45 and 28 Raman and IR frequencies, respectively.

The optical vibrational modes of $Sr_2ZnGe_2O_7$ melilite-type and related materials can be classified as external and internal modes of Ge_2O_7 "pyro" units, rotational and translational modes of the GeO_4 and ZnO_4 units, and translation and libration modes of Sr^{2+} and Zn^{2+}. In this respect, identification of vibrational modes in pyrogermanates has not been fully accomplished despite what we know of vibrational modes in pyrogermanates and related germanates that have been previously studied.[2,53−58] The large number of modes, the mixture of many modes (especially at the low-frequency region), and the lack of known symmetry for the different vibrational modes are the main difficulties found to identify the vibrational modes. Table 4 summarizes the correlation table of the internal and external modes of Ge_2O_7 pyro units between the site group of the molecule (C_{2v}) and the factor group of the crystal (D_{2d}) to help in the identification of the different Raman-active internal modes of the Ge_2O_7 units to be discussed below.

RS spectra of $Sr_2ZnGe_2O_7$ at some representative pressures are shown in Figure 6. The ambient condition Raman and IR spectra of $Sr_2ZnGe_2O_7$ are shown in Supporting Information

Table 4. Correlation Diagram of Symmetries between the Molecular Site Group (C_{2v}) and Solid Factor Group (D_{2d}), Including Its Raman (R) and Infrared (IR) Activity, for Ge_2O_7 Internal and External (translational and librational) Vibrations

assignment	site group symmetry	factor group symmetry
$\nu_s(GeO_3)$	A_1	A_1(R) + B_2(R,IR)
	B_1	E(R,IR)
$\nu_{as}(GeO_3)$	A_1	A_1(R) + B_2(R,IR)
	B_2	E(R,IR)
	B_1	E(R,IR)
	A_2	A_2 + B_1(R)
$\tau(GeO_3)$	A_2	A_2 + B_1(R)
	B_2	E(R,IR)
ν_s(Ge−O−Ge)	A_1	A_1(R) + B_2(R,IR)
ν_{as}(Ge−O−Ge)	B_1	E(R,IR)
δ(Ge−O−Ge)	A_1	A_1(R) + B_2(R,IR)
δ(O−Ge−O)	$3A_1$+$2B_2$+$3B_1$+$2A_2$	$3A_1$(R) + $3B_2$(R,IR)+$2A_2$ +5E(R,IR)+ $2B_1$(R)
L(Ge_2O_7)	A_2+B_1+B_2	A_2 + B_1(R) + 2E(R,IR)
T(Ge_2O_7)	A_1+B_1+B_2	A_1(R)+ B_2(R,IR) + 2E(R,IR)

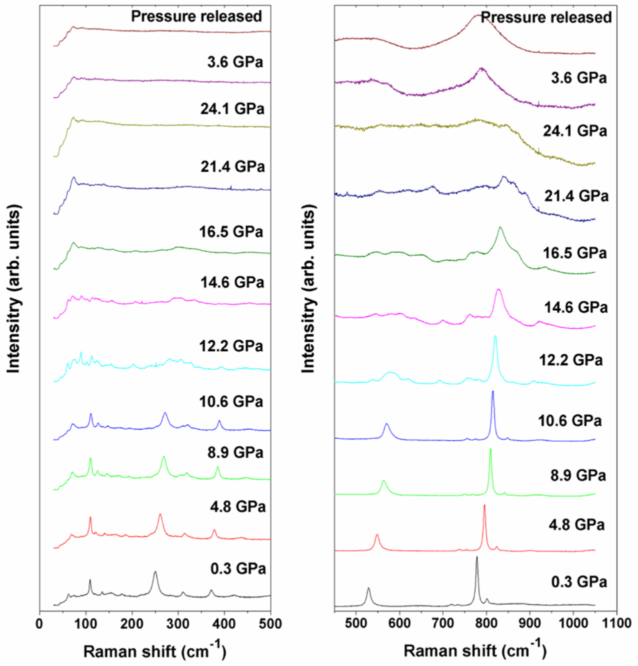

Figure 6. Pressure dependence of Raman scattering spectra of $Sr_2ZnGe_2O_7$ at room temperature.

(Figure S1), where the observed and calculated modes are compared. The ambient pressure RS spectrum of the tetragonal LP phase shows modes and Raman mode frequencies similar to those reported in literature (see Table 5).[2,53] It can be mentioned here that we observed several new modes not previously reported at ambient conditions; however, some of them could not be observed in the DAC experiments at higher pressures. The evolution of RS spectra of $Sr_2ZnGe_2O_7$ at HP shown in Figure 6 indicates that the 16 Raman-active modes observed at ambient pressure persist up to 12 GPa. Only a new mode (around 900 cm^{-1}), not previously observed at lower pressures, starts appearing at ∼4 GPa, and it exists up to 18 GPa. No signature of the commensurate to incommensurate transition is observed at HP in our RS spectra. This agrees well with our assumption of commensurate normal structure for $Sr_2ZnGe_2O_7$. A systematic shift of the modes with pressure is observed with increasing pressure up to 12 GPa. Beyond this pressure several additional modes are observed together with the disappearance of some Raman modes of the LP phase. These changes occur at a similar pressure where the changes in the XRD patterns are noticed and thus give a support to the concluded phase transition in $Sr_2ZnGe_2O_7$ near 12 GPa. The complete RS spectrum of the HP phase is only observed above 17 GPa when all modes of the LP phase have disappeared and only Raman modes of the HP phase remain. Therefore, RS studies show a coexistence of both LP and HP phases at least during 5 GPa, which supports the displacive-type transformation between the two phases. Significant broadening and loss of intensity in RS spectra recorded above 18 GPa make it difficult to follow many Raman modes of the HP phase. At 21 GPa, the modes become very broad, and there is an increase in background, which may be either pressure-induced disorder or amorphization, which might be related to the frustration of a structural transition as seen in most of the framework structure-type materials. In fact, many melilite-type and related compounds are known in glassy (amorphous) state at ambient conditions.[59] The disordered samples could not revert back to the original phase as observed from the RS spectrum of the pressure released sample. It may be noted that the RS spectrum of the recovered sample is similar to those of glassy melilites.[59]

The pressure evolution of the 17 experimental Raman-active mode frequencies of the tetragonal LP phase is shown in Figure 7.The pressure coefficients of the Raman-active modes for the LP phase are obtained by a quadratic fit of experimental data, and they are summarized in Table 5. All the experimental Raman-active modes of the LP phase show a normal positive pressure coefficient in good agreement with our calculations (see Figure 7). With the help of our theoretical calculations, which provide the frequencies, pressure coefficients, and symmetries of the 69 optical vibrations (corresponding to 51 independent frequencies) of the LP phase, we performed a tentative assignment of the symmetry of the 17 experimental Raman-active modes observed (see Table 5). We found that most of the strong Raman-active modes correspond to A_1 symmetry, which is in good agreement with a previous work [namely, ref 48]. Additionally, we tentatively assigned the symmetric or antisymmetric character of stretching (ν), bending (δ), and rocking (τ) modes of the Ge_2O_7 modes with the help of the symmetry of each internal vibration (given in Table 4) and the J-ICE program, which allows to visualize the atomic displacements of each normal vibrational mode as implemented in the Outcar file of the VASP program.[60]

From the analyses of Raman-modes we want to stress a few assignments. First, we assigned the strongest mode of the Raman spectrum (at 777 cm^{-1}) with A_1 symmetry to the $\nu_s(GeO_3)$ mode in good agreement with previous literature.[2,48] Since the other high-frequency mode at 800 cm^{-1} corresponds to the other A_1 mode, Table 4 imposes that this mode must be assigned to the $\nu_{as}(GeO_3)$ mode, which is opposite to the assignment in previous works.[2,53] As regards the bridge Ge−O−Ge modes, the symmetric stretching mode ν_s(Ge−O−Ge) was assigned to the theoretical A_1 and B_2 modes near 500 cm^{-1}. The A_1 mode is responsible for the Raman mode at 528 cm^{-1}, in good agreement with previous literature. Similarly, the bending δ(Ge−O−Ge) modes were assigned to theoretical A_1

Table 5. Theoretical and Experimental Optical Mode Frequencies, Their Pressure Coefficients, and Mode Gruneisen Parameters in the Tetragonal Low-Pressure Phase of $Sr_2ZnGe_2O_7$[a] as Fitted to Equation $\omega(P) = \omega_0 + aP + bP^2$

sym	character	ω_0 (theor) (cm^{-1})	a (theor) (cm^{-1}/GPa)	b (theor) (cm^{-1}/GPa^2)	ω_0(exp) (cm^{-1})	a (exp) (cm^{-1}/GPa)	b (exp) (cm^{-1}/GPa^2)
$1B_1$*	T(Sr+Zn)	59.0	2.71	−0.180			
2E**	T(Sr+Zn+Ge)	62.5	2.23	−0.110			
$3A_2$	L(Ge_2O_7)+ T(Sr+Zn)	64.4	6.64	−0.200			
4E**	T(Sr+Zn+Ge_2O_7)	102	3.77	−0.120			
5E**	T(Sr+Zn+Ge_2O_7)	104	0.10		109	0.15	−0.005
$6A_1$*	T(Sr+Ge)	108	2.98	−0.130			
7E**	T(Sr+Zn)	116	2.08	−0.040			
$8B_1$*	T(Sr+Zn)	118	0.53	−0.015	118	0.83	−0.001
$9B_1$*	δ(O−Ge−O)+T(Sr)	126	1.78	0.020			
$10A_1$*	T(Sr+Ge_2O_7)	131	1.24	−0.020	135	0.94	0.020
$11B_2$**	T(Sr+Zn)	132	1.22	−0.030			
$12A_2$	δ(O−Ge−O)+T(Sr)	137	0.43				
13E**	L(Ge_2O_7) +T(Sr+Zn)	143	1.75				
$14A_1$*	T(Sr+Ge_2O_7)	154	2.07	−0.040	154	1.90	−0.010
$15B_2$**	T(Sr+Zn+Ge_2O_7)	156	2.85	−0.020			
16E**	δ(O−Ge−O) +T(Sr+Zn)	173	1.90	−0.040	178	1.74	−0.018
17E**	L(Ge_2O_7) +T(Sr+Zn)	190	4.81	−0.160			
$18B_2$**	T(Sr+Zn+Ge_2O_7)	196	3.85	−0.090			
$19A_2$	L(Ge_2O_7)	208	3.10				
20E**	δ(O−Ge−O)+T(Sr+Zn +Ge)	210	2.07				
$21A_1$*	δ(O−Ge−O)+T(Sr)	211	5.91	−0.070			
$22B_1$*	L(Ge_2O_7)	217	2.38				
$23B_2$**	δ(O−Ge−O)+T(Sr)	220	2.79	−0.030	225	3.58	−0.090
24E**	δ(O−Ge−O)	237	3.02	−0.090			
$25A_1$*	δ(O−Ge−O)	245	2.72		250	2.55	−0.050
26E**	δ(O−Ge−O)+T(Zn)	268	2.22	0.060			
$27B_2$**	δ(O−Ge−O)	273	3.83	−0.030			
$28B_1$*	δ(O−Ge−O)	293	0.93	0.030	310	0.66	0.200
29E**	δ(O−Ge−O)	298	2.44	0.020			
$30A_2$	δ(O−Ge−O)	300	0.91				
$31A_1$*	δ(O−Ge−O)	352	1.89	0.008	371	1.09	0.050
32E**	δ(O−Ge−O)	393	2.74	−0.040			
$33B_2$**	δ(O−Ge−O)	397	3.74	−0.030	418	4.09	−0.100
$34B_1$*	τ(GeO_3)	411	8.52	−0.120			
35E**	τ(GeO_3)+v_{as}(ZnO_4)	442	7.42	−0.100			
$36A_2$	τ(GeO_3)+v_s(ZnO_4)	452	5.77	−0.030			
$37A_1$*	ν_s(Ge−O−Ge)	458	5.34	−0.120			
$38B_2$**	ν_s(Ge−O−Ge)	471	5.58	−0.130			
39E**	δ(O−Ge−O)+ v_{as}(ZnO_4)	489	5.81	−0.070			
$40B_2$**	δ(Ge−O−Ge)	493	4.23	−0.016			
$41A_1$*	δ(Ge−O−Ge)+ v_s(ZnO_4)	509	4.57	−0.040	528	4.42	−0.040
42E**	ν_{as}(GeO_3)	676	4.16	−0.090	718	4.24	−0.050
43E**	ν_{as}(GeO_3)	677	4.28	−0.070	718	4.24	−0.050
$44B_1$*	ν_{as}(GeO_3)	694	4.50	−0.080	734	4.12	−0.020
$45B_2$*	ν_s(GeO_3)	736	4.27	−0.070			
46E**	ν_s(GeO_3)	738	5.34	−0.060			
$47A_1$*	ν_s(GeO_3)	739	4.16	−0.060	777	3.94	−0.030
$48B_2$*	ν_{as}(GeO_3)	752	5.00	−0.060			
$49A_2$	ν_{as}(GeO_3)	753	4.33	−0.080			
$50A_1$*	ν_{as}(GeO_3)	762	5.04	−0.060	800	5.18	−0.060
51E**	ν_{as}(Ge−O−Ge)	815	8.83	−0.130	872[b]	5.43	−0.002

[a] Information regarding Raman (*) or Raman and infrared (**) activity is also provided. [b] Reference 2; value extrapolated to zero pressure from experimental linear pressure coefficient.

and B_2 modes at 245 and 273 cm^{-1}. Another A_1 mode is responsible for the Raman mode at 250 cm^{-1} in good agreement with literature. On the other hand, the antisymmetric stretching mode ν_{as}(Ge−O−Ge) was assigned to the theoretical E mode at 815 cm^{-1}, which has a very large pressure coefficient. This assignment also is in good agreement with literature.[53,56,58] We attributed this mode to the weak Raman mode observed above 4 GPa. This assignment is in good

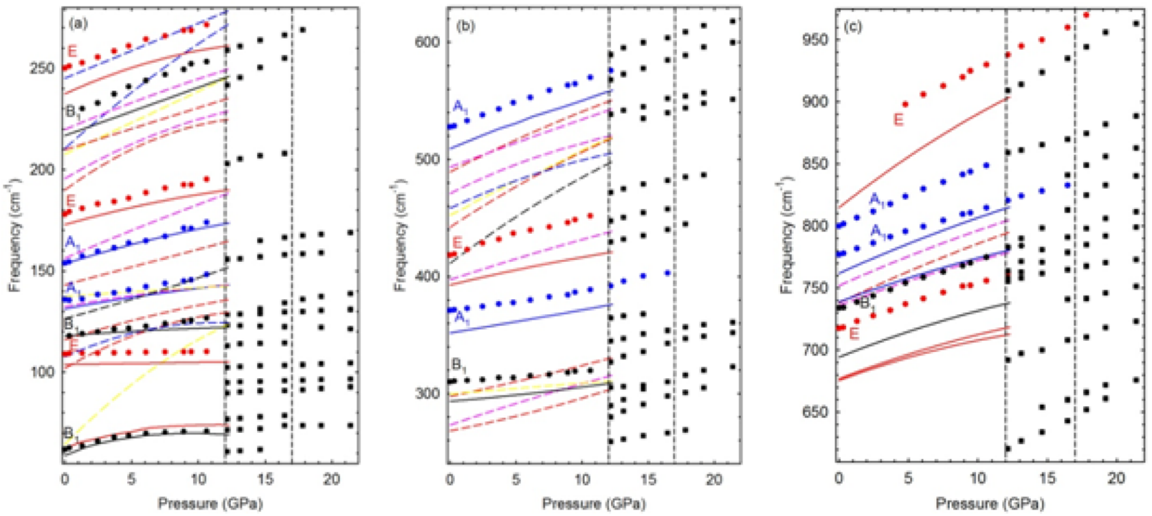

Figure 7. Pressure dependence of Raman-active mode frequencies of tetragonal LP and monoclinic HP phases of $Sr_2ZnGe_2O_7$: (a) low-frequency region; (b) medium-frequency region; (c) high-frequency region. Experimental data of LP (HP) phase are depicted with ● (■). Solid (dashed) lines correspond to theoretical Raman modes of the LP phase identified (not identified) with experimentally observed modes. Black, red, blue, pink, and yellow refer to vibrational modes of the LP phase with B_1, E, A_1, B_2, and A_2 symmetry, respectively.

Table 6. Raman-Active Mode Frequencies and Pressure Coefficients for the Monoclinic High-Pressure Phase of $Sr_2ZnGe_2O_7$ at 12.2 GPa as Fitted to Equation $\omega(P) = \omega_{12.2} + a(P - 12.2) + b(P - 12.2)^2$

	$\omega_{12.2}$ (cm^{-1})	a (cm^{-1}/GPa)	b (cm^{-1}/GPa^2)		$\omega_{12.2}$ (cm^{-1})	a (cm^{-1}/GPa)	b (cm^{-1}/GPa^2)
ω_1	60.8	0.56	−0.050	ω_{21}	365	2.19	−0.300
ω_2	71.3	0.64	−0.040	ω_{22}	430	1.63	0.200
ω_3	76.7	0.55	−0.030	ω_{23}	447	3.63	−0.30
ω_4	89.9	0.26	−0.005	ω_{24}	472	2.93	−0.100
ω_5	95	0.22	−0.003	ω_{25}	526	3.95	−0.100
ω_6	103	0.23	−0.002	ω_{26}	538	3.35	−0.100
ω_7	113	0.78	−0.100	ω_{27}	568	4.41	−0.100
ω_8	123	−0.11	−0.007	ω_{28}	590	3.91	−0.100
ω_9	126	2.35	−0.010	ω_{29}	621	4.76	0.100
ω_{10}	128	0.29	−0.001	ω_{30}	641	5.34	−0.200
ω_{11}	156	0.61	−0.020	ω_{31}	693	3.57	−0.020
ω_{12}	162	1.22	−0.060	ω_{32}	741	−1.15	0.200
ω_{13}	203	2.23	−0.300	ω_{33}	756	2.62	−0.080
ω_{14}	242	4.23	−0.300	ω_{34}	758	5.44	−0.100
ω_{15}	259	2.05	−0.060	ω_{35}	764	7.52	−0.300
ω_{16}	280	4.98	−0.200	ω_{36}	782	8.53	−0.200
ω_{17}	290	6.12	−0.300	ω_{37}	804	10.56	−0.450
ω_{18}	305	1.08	−0.200	ω_{38}	859	2.36	0.100
ω_{19}	327	4.53	−0.200	ω_{39}	908	7.06	−0.100
ω_{20}	345	2.67	−0.100				

agreement with its weak Raman intensity since this mode is very strong in IR. The ambient-pressure IR modes are similarly assigned as 813 cm^{-1} (ν_{as}(Ge−O−Ge)), 779 and 727 cm^{-1} ($\nu_{as}(GeO_3)$, 526 cm^{-1} (δ(Ge−O−Ge), 486 cm^{-1} (δ(Ge−O−Ge), $\nu_{as}(GeO_4)$, and ν_{as}(Ge−O−Ge)), and 445 cm^{-1}(τ(GeO3) and $\nu_{as}(GeO_4)$).

Finally, regarding the modes of the HP phase, RS spectra recorded above 12.2 GPa show splitting of several modes in addition to the appearance of new modes at 545, 650, and 717 cm^{-1} other than the modes due to the tetragonal LP phase, which persist up to 17 GPa. The frequencies and pressure coefficients of the Raman modes attributed to the HP phase at 12.2 GPa are given in Table 6. Group theoretical analysis of the monoclinic HP phase ($P2_1/n$; point group: C_{2h}) predicts 72 Raman modes with mechanical representation: $\Gamma = 36A_g + 36B_g$.Therefore, the appearance of more Raman-active modes in the HP structure than in the LP structure is consistent with the decrease of symmetry observed by XRD studies. Other possible structures with monoclinic symmetry for melilite-type materials as observed for $Ba_2MgSi_2O_7$ ($C2/c$, point group: C_{2h}) predict a smaller number (39) Raman-active modes with mechanical representation: $\Gamma = 17A_g + 19Bg$. Since the number of observed Raman-active modes is below 39, it is not possible to confirm the symmetry from Raman data alone. The pressure dependencies of Raman modes of HP phase were also fitted by a linear relation, and the pressure coefficients of Raman modes are given in Table 6. The monoclinic HP phase exhibits one soft mode at 123 cm^{-1}. In this respect, the analysis of the Raman mode frequencies suggests that the internal modes of Ge_2O_7 and ZnO_4 units of the LP and HP phases become stiffer with increasing pressure, while the low-frequency modes (mainly due to translation of the Sr^{2+}) become softer in the HP phase, likely prior to amorphization. This feature is consistent with the strong local distortion of the SrO_8 polyhedra induced by pressure in melilite-type materials and rigidity of GeO_4 tetrahedral units. Furthermore, the highest frequency mode of the HP phase has a slightly smaller frequency than that of the LP phase, the antisymmetric bridge stretching not observed at ambient pressure (see Figure 7). Therefore, the frequency decrease of the highest Raman-active mode in the HP phase compared to the LP phase suggests a possible small increase of coordination in the tetrahedral cations of the HP phase, as indeed observed for Zn atoms according to parameters obtained from XRD data.

V. CONCLUSION

A new reversible transition from tetragonal to monoclinic structure in $Sr_2ZnGe_2O_7$ near 12 GPa is delineated from the ambient and in situ HP XRD and RS investigations. The HP monoclinic phase resulted from a slight displacement of atoms and has closely related structural arrangements to those of the parent low-pressure tetragonal phase. The bulk modulus and its pressure derivative for the LP tetragonal phase are found to be 85(6) GPa and 6.1(8), respectively, while those of HP phase are 88.6 GPa and 4.29, respectively. The pressure evolution of both LP and HP phases in $Sr_2ZnGe_2O_7$ indicates a feeble structural change with a volume drop of ~1%. Both LP and HP phases show anisotropic compressibility with larger compression along the stacking direction of $[ZnGe_2O_7]^{2-}$ sheets. Our lattice dynamics investigations have followed the pressure dependence of 17 Raman-active modes of the LP phase and support the phase transition observed near 12 GPa. A comparison with all the theoretically expected Raman-active modes for the tetragonal phase have allowed us to give a tentative assignment of the symmetries and character of experimental frequencies, mainly, to those corresponding to relatively high-frequency Raman-active modes. Raman-active modes of the high-pressure phase have also been measured up to 21 GPa. A soft Raman-active mode observed in the high-pressure phase was related to the amorphization of $Sr_2ZnGe_2O_7$ as suggested by the broadening of Raman spectra above 21 GPa.

■ ASSOCIATED CONTENT

Ⓢ Supporting Information

Typical Raman and infrared spectra of $Sr_2ZnGe_2O_7$ at ambient conditions. The observed and DFT-calculated modes are shown. The Supporting Information is available free of charge on the ACS Publications website at DOI: 10.1021/acs.inorgchem.5b00937.

■ AUTHOR INFORMATION

Corresponding Author

*Phone: 0092-22-25592328. Fax: 0091-22-25505151. E-mail sachary@barc.gov.in or acharysn@rediffmail.com.

Author Contributions

The manuscript was written through contributions of all authors. All the authors have equal contribution to this manuscript. All authors have given approval to the final version of the manuscript.

Notes

The authors declare no competing financial interest.

■ ACKNOWLEDGMENTS

Research supported by the Spanish government MINECO under Grant Nos. MAT and CSD2007-00045 and MAT2013-46649-C4-1/2/3-P. S.N.A. acknowledges the support provided by Universitat de Valencia during his visit there.

■ REFERENCES

(1) Kaminskii, A. A. *Laser Photonics Rev.* **2007**, *1*, 93−177.

(2) Becker, P.; Bohaty, L.; Liebertz, J.; Kleebe, H.-J.; Muller, M.; Eichler, H. J.; Rhee, H.; Hanuza, J.; Kaminskii, A. A. *Laser Phys. Lett.* **2010**, *7*, 367−377.

(3) Kuang, X.; Green, M.; Niu, H.; Zajdel, P.; Dickinson, C.; Claridge, J. B.; Jantsky, L.; Rosseinsky, M. J. *Nat. Mater.* **2008**, *7*, 498−504.

(4) Adams, R. D.; Layland, R.; Payen, C.; Datta, T. *Inorg. Chem.* **1996**, *35*, 3492−3497.

(5) Ambruster, T.; Rothklisberger, F.; Seifert, F. *Am. Mineral.* **1990**, *75*, 847−858.

(6) Fahey, A. J.; Zinner, E. K.; Crozaz, G.; Kornacki, A. S. *Geochim. Cosmochim. Acta* **1987**, *51*, 3215−3229.

(7) Hayashi, T.; Muehlenhachs, K. *Geochim. Cosmochim. Acta* **1986**, *50*, 585−591.

(8) Grossman, L. *Geochim. Cosmochim. Acta* **1975**, *39*, 433−454.

(9) Kaminskii, A. A.; Bohatý, L.; Becker, P.; Liebertz, J.; Held, P.; Eichler, H. J.; Rhee, H.; Hanuza, J. *Laser Phys. Lett.* **2008**, *5*, 845−868.

(10) Gudfinnsson, G. H.; Presnall, D. C. *J. Petrol.* **2005**, *46*, 1645−1659.

(11) Bindi, L.; Bonazzi, P. *Phys. Chem. Miner.* **2003**, *30*, 523−526.

(12) Bindi, L.; Bonazzi, P. *Phys. Chem. Miner.* **2005**, *32*, 89−96.

(13) Jia, Z. H.; Schaper, A. K.; Massa, W.; Treutmanna, W.; Rager, H. *Acta. Crystallogr., Sect. B* **2006**, *62*, 547−555.

(14) Jiang, J. C.; Schosnig, M.; Schaper, A. K.; Ganster, K.; Rager, H.; Tóth, L. *Phys. Chem. Miner.* **1998**, *26*, 128−134.

(15) Bagautdinov, B.; Hagiya, K.; Noguchi, S.; Ohmasa, M.; Ikeda, N.; Kusaka, K.; Iishi, K. *Phys. Chem. Miner.* **2002**, *29*, 346−350.

(16) Swainson, I. P.; Dove, M. T.; Schmahl, W. W.; Putnis, A. *Phys. Chem. Miner.* **1992**, *19*, 185−195.

(17) Peters, L.; Knorr, K.; Knapp, M.; Depmeier, W. *Phys. Chem. Miner.* **2005**, *32*, 546−551.

(18) Merlini, M.; Gemmi, M.; Hanfland, M.; Crichton, W. *Am. Miner.* **2009**, *94*, 704−709.

(19) Seifert, F.; Czank, M.; Simons, B.; Schmahl, W. *Phys. Chem. Miner.* **1987**, *14*, 26−35.

(20) Bindi, L.; Bonazzi, P.; Dusĺek, M.; Petrõcek, V.; Chapuis, G. *Acta. Crystallogr., Sect. B* **2001**, *57*, 739−746.

(21) Yang, H.; Hazen, R. M.; Downs, R. T.; Finger, L. W. *Phys. Chem. Miner.* **1997**, *24*, 510−519.

(22) Merlini, M.; Gemmi, M.; Artioli, G. *Phys. Chem. Miner.* **2005**, *32*, 189−196.

(23) Merlini, M.; Gemmi, M.; Cruciani, G.; Artioli, G. *Phys. Chem. Miner.* **2008**, *35*, 147−155.

(24) Ardit, M.; Zanelli, C.; Dondi, M.; Cruciani, G. *Period. Mineral.* **2011**, *80*, 155−165.

(25) Ardit, M.; Dondi, M.; Merlini, M.; Cruciani, G. *Phys. Chem. Miner.* **2012**, *39*, 199−211.

(26) Bakakin, V. V.; Belov, V. V.; Borisov, S. V.; Soloveyeva, L. P. *Am. Mineral.* **1970**, *55*, 1167−1181.

(27) Kraus, W.; Nolze, G. *J. Appl. Crystallogr.* **1996**, *29*, 301−303.

(28) Rodriguez-Carvajal, J. *Fullprof 2000,* A program for Rietveld, profile matching and integrated intensity refinements for X-ray and Neutron data, Version 1.6; Laboratoire Leon Brillouin: Gif sur Yvette, France, 2000.

(29) Kresse, G.; Furthmuller, J. *Phys. Rev. B* **1996**, *54*, 11169−11186.

(30) Perdew, J. P.; Ruzsinszky, A.; Csonka, G. I.; Vydrow, O. A.; Scuseria, G. E.; Constantin, L. A.; Zhou, X.; Burke, K. *Phys. Rev. Lett.* **2008**, *100*, 136406.

(31) Kresse, G.; Joubert, D. *Phys. Rev. B* **1999**, *59*, 1758−1775.

(32) Monkhorst, H. J.; Pack, J. D. *Phys. Rev. B* **1976**, *13*, 5188−5192.

(33) Mujica, A.; Rubio, A.; Muñoz, A.; Needs, R. *Rev. Mod. Phys.* **2003**, *75*, 863.
(34) Parlinski, K. *computer code PHONON*; Polish Academy of Sciences: Cracow, Poland, 2010. Online: http://wolf.ifj.edu.pl/phonon/.
(35) Becker, P.; Held, P.; Liebertz, J.; Bohatý, L. *Cryst. Res. Technol.* **2009**, *44*, 603−612.
(36) Ochi, Y.; Tanaka, K.; Morikawa, H. *J. Mineral. Soc. Japan* **1982**, *15*, 331−341.
(37) Aitasalo, T.; Hölsä, J.; Laamanen, T.; Lastusaari, M.; Lehto, L.; Niittykoski, J.; Pellé, F. *Z. Kristallogr.* **2006**, *23*, 481−486.
(38) Errandonea, D.; Gomis, O.; García-Domene, B.; Pellicer-Porres, J.; Katari, V.; Achary, S. N.; Tyagi, A. K.; Popescu, C. *Inorg. Chem.* **2013**, *52*, 12790−12798.
(39) Bandiello, E.; Errandonea, D.; Martinez-Garcia, D.; Santamaria-Perez, D.; Manjon, F. J. *Phys. Rev. B* **2012**, *85*, 024108.
(40) Errandonea, D.; Kumar, R. S.; Gracia, L.; Beltran, A.; Achary, S. N.; Tyagi, A. K. *Phys. Rev. B* **2009**, *80*, 094101.
(41) Gracia, L.; Beltran, A.; Errandonea, D. *Phys. Rev. B* **2009**, *80*, 094105.
(42) Angel, R. J.; Bujak, M.; Zhao, J.; Gatta, G. D.; Jacobsen, S. D. *J. Appl. Crystallogr.* **2007**, *40*, 26−32.
(43) Klotz, S.; Chervin, J. C.; Munsch, P.; Marchand, G. L. *J. Phys. D: Appl. Phys.* **2009**, *42*, 075413.
(44) Errandonea, D.; Meng, Y.; Somayazulu, M.; Häusermann, D. *Phys. B* **2005**, *355*, 116−125.
(45) Garg, A. B.; Errandonea, D.; Rodriguez-Hernandez, P.; Lopez-Moreno, S.; Muñoz, A.; Popescu, C. *J. Phys.: Condens. Matter* **2014**, *26*, 265402.
(46) Ruiz-Fuertes, J.; Errandonea, D.; Lacomba-Perales, R.; Segura, A.; Gonzalez, J.; Rodriguez, F.; Manjon, F. J.; Ray, S.; Rodriguez-Hernandez, P.; Muñoz, A.; Zhu, Z.; Tu, C.-Y. *Phys. Rev. B* **2010**, *81*, 224115.
(47) Trunov, V. K.; Oboznenko, Y. U.; Sirotinkin, S. P.; Tskhelashvili, N. B. *Izv. Akad. Nauk SSSR, Neorg. Mater.* **1991**, *27*, 1993−1994.
(48) Redhammer, G. J.; Roth, G. *Acta. Crystallogr., Sect. C* **2006**, *62*, i61−i63.
(49) Errandonea, D.; Ferrer-Roca, Ch.; Martínez-Garcia, D.; Segura, A.; Gomis, O.; Muñoz, A.; Rodríguez-Hernández, P.; López-Solano, J.; Alconchel, S.; Sapiña, F. *Phys. Rev. B* **2010**, *82*, 174105.
(50) Errandonea, D.; Santamaría-Perez, D.; Vegas, A.; Nuss, J.; Jansen, M.; Rodríguez-Hernandez, P.; Muñoz, A. *Phys. Rev. B* **2008**, *77*, 094113.
(51) Gomis, O.; Sans, J. A.; Lacomba-Perales, R.; Errandonea, D.; Meng, Y.; Chervin, J. C.; Polian, A. *Phys. Rev. B* **2012**, *86*, 054121.
(52) Errandonea, D.; Kumar, R. S.; Ma, X.; Tu, C. *J. Solid State Chem.* **2008**, *181*, 355−364.
(53) Hanuza, J.; Maczka, M.; Ptak, M. *J. Raman Spectrosc.* **2011**, *42*, 782−789.
(54) Hanuza, J.; Jezowska-Trzebiatowska, B.; Lukaszewicz, K. *J. Mol. Struct.* **1972**, *13*, 391−403.
(55) Tarte, P.; Pottier, M. J.; Procès, A. M. *Spectrochim. Acta, Part A* **1973**, *29*, 1017−1027.
(56) Gabelica-Robert, M.; Tarte, P. *Spectrochim. Acta, Part A* **1979**, *35*, 649−654.
(57) Saez-Puche, R.; Bijkerk, M.; Fernández, F.; Baran, E. J.; Botto, I. L. *J. Alloys Comp.* **1992**, *184*, 25−34.
(58) Baran, E. J.; Cascales, C. *J. Raman Spectrosc.* **1999**, *30*, 77−79.
(59) Sharma, S. K.; Yoder, H. S., Jr.; Matson, D. W. *Geochim. Cosmochim. Acta* **1988**, *52*, 1961−1967.
(60) Canepa, P.; Hanson, R. M.; Ugliengo, P.; Alfredsson. *J. Appl. Crystallogr.* **2011**, *44*, 225−229.